European Journal of Pharmaceutical Sciences 217 (2026) 107402

Contents lists available at ScienceDirect

European Journal of Pharmaceutical Sciences

journal homepage: www.elsevier.com/locate/ejps

Longitudinal monitoring of nanofibrillar cellulose hydrogel medical implants in mice using positron emission tomography

Xiaoqing Zhuang [a,b,c], Jenni Virta [a], Heidi Liljenbäck [a], Lauri Paasonen [d], Anu J. Airaksinen [a,b,c], Anne Roivainen [a,c,e,f], Xiang-Guo Li [a,b,c,e,*]

[a] Turku PET Centre, University of Turku, Turku, Finland
[b] Department of Chemistry, University of Turku, Turku, Finland
[c] Turku PET Centre, Turku University Hospital, Turku, Finland
[d] UPM Biomedicals, UPM Inc., Helsinki, Finland
[e] InFLAMES Research Flagship Center, University of Turku, Finland
[f] Turku Center for Disease Modeling, University of Turku, Turku, Finland

ARTICLE INFO

Keywords:
Medical implantation
Hydrogel
Nanofibrillar cellulose
PET
Radiolabeling
Zirconium-89

ABSTRACT

Nanofibrillar cellulose (NFC) hydrogel has emerged as a promising implantable material for therapeutic applications. In this study, the relatively longer-lived positron-emitting radionuclide zirconium-89 was chelated to the octadentate deferoxamine (DFO*)-conjugated NFC hydrogel ([^{89}Zr]Zr-DFO*-NFC) to enable longitudinal monitoring of its *in vivo* fate using positron emission tomography techniques. Following subcutaneous implantation in healthy mice, [^{89}Zr]Zr-DFO*-NFC retained radioactivity at the implant site for at least 14 days, with minimal signal detected in the kidneys, urinary bladder, and overlying skin. In contrast, mice receiving a control formulation of [^{89}Zr]Zr-oxalate mixed with NFC hydrogel showed progressive accumulation of radioactivity in the bones, consistent with known [^{89}Zr]Zr-oxalate distribution patterns, and only limited retention at the implant site by Day 7. These findings demonstrate that [^{89}Zr]Zr-DFO*-NFC hydrogel implants exhibit high *in vivo* stability with negligible systemic release following subcutaneous implantation, supporting their potential use as safe and traceable biomaterial platforms.

1. Introduction

Nanofibrillar cellulose (NFC) is a sustainably available biomaterial derived from plants that is biocompatible for controlled drug release and three dimensional (3D) cell culturing (Wang et al., 2021). NFC hydrogel consists of cellulose and hemicellulose macromolecules dispersed in water, forming a physically entangled nanofiber network. Unlike polymerized or chemically cross-linked hydrogels, NFC relies on hydrogen bonding and van der Waals interactions between nanofibers to maintain its structure. This imparts distinctive rheological properties, including shear-thinning behavior: viscosity decreases under shear stress, allowing the hydrogel to temporarily liquefy during injection and rapidly recover its semi-solid state once the stress is removed. This characteristic facilitates minimally invasive administration and implantation—NFC can be injected through needles or extruded via bioprinting devices before resolidifying into stable, porous structures that mimic the extracellular matrix and support cell growth and tissue integration (Malekpour et al., 2023; Sultan et al., 2017). In addition to the large literature data from preclinical studies, the emergence of clinical data further supports potential applications for medical care. For example, NFC has been used to facilitate skin wound healing in 24 patients, and promising clinical benefits have been observed (Koivuniemi et al., 2020).

The NFC hydrogel is primarily composed of cellulose, a linear glucose polymer linked by β−1,4-glycosidic bonds. Its typical carbohydrate composition is 72.8 % glucose, 25.6 % xylose, and 1.4 % mannose, reflecting a dominant cellulose fraction with minor hemicellulose contributions. Because most mammals, including humans, lack cellulase enzymes capable of cleaving β-1,4 linkages, NFC hydrogel degrades slowly *in vivo* (Mishra et al., 2022). Thus, the implanted NFC hydrogel is not expected to spontaneously fragment or decompose, although chemical modifications can be introduced to accelerate degradation if desired. Combining these features with its stability and tunability makes NFC hydrogel a strong candidate for subcutaneous (s.c.) implantation in therapeutic applications.

* Corresponding author at: Turku PET Centre, Kiinamyllynkatu 4-8, FI-20520 Turku, Finland.
E-mail address: xiali@utu.fi (X.-G. Li).

https://doi.org/10.1016/j.ejps.2025.107402
Received 11 October 2025; Received in revised form 1 December 2025; Accepted 5 December 2025
Available online 6 December 2025

Understanding the *in vivo* fate of implantable biomaterials is essential for evaluating their stability, degradation, and host interactions. NFC hydrogels are expected to be biocompatible and should not elicit strong immune responses that compromise material integrity and safety. Noninvasive imaging has emerged as a powerful tool to longitudinally assess biomaterials *in vivo*, providing quantitative, evidence-based insights while reducing experimental risks (Gil et al., 2019; Pawelec et al., 2024). For example, the stability of technetium-99m (^{99m}Tc)-labeled NFC hydrogel was previously evaluated using single-photon emission computed tomography/computed tomography (SPECT/CT), where the material remained stable for at least 5 h in mice (Laurén et al., 2014). However, *in vivo* monitoring data from longer periods and detailed *ex vivo* biodistribution data remain limited.

Positron emission tomography (PET) offers superior sensitivity (fM to nM), penetration of deep tissues, and quantitative capability, enabling longitudinal and whole-body tracking of radiolabeled biomaterials. When combined with *ex vivo* gamma counting, PET provides a robust platform for assessing implant stability and systemic distribution. Zirconium-89 (^{89}Zr), a positron-emitting radionuclide with a physical half-life of 78.4 h (3.3 d), is well suited for long-term imaging studies. For radiolabeling, ^{89}Zr requires a stable chelator, and the next-generation desferrioxamine derivative DFO*, currently under clinical evaluation, forms one of the most stable complexes with $^{89}Zr^{4+}$ (Feiner et al., 2021). In this study, we employed PET imaging and *ex vivo* biodistribution quantification to investigate the stability and *in vivo* fate of s.c. implanted [^{89}Zr]Zr-DFO*-NFC hydrogels in healthy mice, aiming to generate key data to support future clinical development of NFC-based biomaterials as a controlled drug release platform.

2. Materials and methods

2.1. General information

Reagents and solvents were mainly purchased from Sigma-Aldrich and Merck and used without further purification. NFC hydrogel was provided by UPM Biomedicals, Helsinki, Finland. ^{89}Zr-radionuclide was purchased via Revvity Oyj (Turku, Finland; manufactured by BV Cyclotron VU, Amsterdam, The Netherlands). All radiation work was conducted in accordance with the guidelines established by the Finnish Radiation and Nuclear Safety Authority (STUK).

2.2. Preparation of DFO*-NFC

The conjugation of DFO* to NFC was performed following published protocols (Feiner et al., 2021; Leppiniemi et al., 2021). NFC hydrogel (350 mg), containing 3 % NFC hydrogel in water (UPM Biomedicals) was transferred to 2-mL LoBind® Eppendorf tubes and diluted with deionized water under magnetic stirring. Freshly prepared aqueous solutions of *N*-hydroxysuccinimide (NHS) at a final concentration of 125 mM (Merck) and 1-ethyl-3-(3-dimethylaminopropyl)carbodiimide (EDC) hydrochloride at a final concentration of 50 mM (Merck) were sterile-filtered with 0.2 μm filters, mixed, and added to the NFC hydrogel solution. The reaction mixture was vigorously stirred at room temperature (RT) for 15 min to activate the carboxyl groups on the NFC surface. Subsequently, the chelator DFO* (ABX, Radeberg, Germany) dissolved in dimethyl sulfoxide (DMSO) at 10 mg/mL (21 μL) was added to the activated NFC solution to achieve a final NFC concentration of 1 %. The conjugation reaction mixture was kept at RT for 2 h under continuous stirring. The reaction was quenched by adding Tris–HCl buffer (pH 8.0, final concentration 20 mM). After removing the magnetic stirring bar, the mixture was centrifuged at 14,000 × *g* for 40 min to pellet the DFO*-NFC hydrogel. The obtained DFO*-NFC hydrogel was washed twice with deionized water and centrifuged to concentrate. The supernatant samples from the final wash were analyzed by high-performance liquid chromatography (HPLC) using a LC-40D device (Shimadzu, Kyoto, Japan).

2.3. Preparation of [^{89}Zr]Zr-DFO*-NFC

^{89}Zr-radiolabeling was performed following established protocols with some modifications (Chomet et al., 2021). The stock solution of [^{89}Zr]Zr-oxalate in 1.0 M oxalic acid (173.0 MBq, 119 μL) was diluted with 1.0 M oxalic acid (554 μL, Sigma-Aldrich, Burlington, MA, USA). The pH of [^{89}Zr]Zr-oxalate solution was adjusted to 7–8 by addition of Na_2CO_3 (Merck, Darmstadt, Germany) solution (2.0 M, 303 μL) and allowing to react for 3 min. The DFO*-NFC hydrogel (240 mg) was transferred to an Eppendorf tube with 271 μL of 4-(2-hydroxyethyl)-1-piperazineethanesulfonic acid (HEPES) buffer (pH 7.1, 0.5 M) supplied from Merck and mixed well with magnetic stirring. A pre-mixed solution of [^{89}Zr]Zr-oxalate (150 μL, 25.5 MBq, pH 7 − 8) and HEPES buffer (79 μL, pH 7.1) was then added to the DFO*-NFC hydrogel suspension. The reaction mixture was stirred vigorously at RT for 1 h. Following incubation, the reaction mixture was centrifuged at 14,000 × *g* for 40 min, and the supernatant was discarded. The product [^{89}Zr]Zr-DFO*-NFC was washed twice with sterile water and collected by centrifugation. Quality control was performed by measuring the pH of the final product with pH paper strips (Whatman, Little Chalfont, UK) and determining the radiochemical purity of [^{89}Zr]Zr-DFO*-NFC using silica gel thin-layer chromatography (TLC) on Silica Gel 60 F254 aluminum-backed plates (Merck, Darmstadt, Germany). The mobile phase for TLC development was 2,2′,2″,2‴-(ethane-1,2-diyldinitrilo)tetraacetic acid (EDTA, Sigma-Aldrich, Burlington, MA, USA) in water (50.0 mM, pH 4.6).

To determine the shelf-life of [^{89}Zr]Zr-DFO*-NFC, the radiochemical purity was measured at 1, 2, 3, 12, and 24 h post-labeling using TLC. The stability of [^{89}Zr]Zr-DFO*-NFC in phosphate-buffered saline (PBS) was also evaluated over 24 h by TLC. For stability testing, PBS was added to [^{89}Zr]Zr-DFO*-NFC at 1:1 (*v/v*) ratio and incubated at RT. The mixture was centrifuged at every time point (1, 2, 3, 12, and 24 h) to separate the supernatant and sediment, and the radiochemical purity of each fraction was determined by TLC.

2.4. Preparation of [^{89}Zr]Zr-oxalate and NFC hydrogel mixture

For the control experiments, a mixture of [^{89}Zr]Zr-oxalate and NFC hydrogel was prepared. Accordingly, NFC hydrogel (1.0 g) was mixed with [^{89}Zr]Zr-oxalate solution (40.8 MBq, 125 μL, pH 7 − 8) without chemical conjugation. The pH of the end product was measured using pH paper strips.

2.5. Animals

All animal experiments were performed in accordance with ARRIVE guidelines and European Union Directive 2010/EU/63 on the protection of animals used for scientific purposes and were approved by the Finnish National Project Authorisation Board (license number ESAVI/15087/2023).

This preclinical study was conducted without randomization or blinding due to its exploratory nature and small sample size. Healthy male C57BL/6NHsd mice (n = 10, aged 6 weeks) of specific pathogen-free quality (Inotiv, Horst, The Netherlands) were used. Animals were allowed a 5-day acclimatization period before the experimental procedures. Mice were housed at RT (18−24 °C) and relative humidity of 40−70 %. Lighting was artificial with a 12-h light/dark cycle (lights off 19:00–07:00). The animals received regular chow (Teklad Global Diet 2018C, Inotiv) and tap water *ad libitum*. The cages contained aspen bedding (Tapvei, Harjumaa, Estonia) and standard environmental enrichment materials, including polycarbonate tunnels and shelters, soft paper nesting material (cellulose wadding, Abena, Växsjö, Sweden), wooden chew sticks (aspen S-bricks, Tapvei), and wood shavings. Mice were randomly divided into two groups for s.c. implantation of either [^{89}Zr]Zr-DFO*-NFC hydrogel (Group A) or [^{89}Zr]Zr-oxalate mixed with NFC hydrogel (Group B). In each group, four animals underwent serial

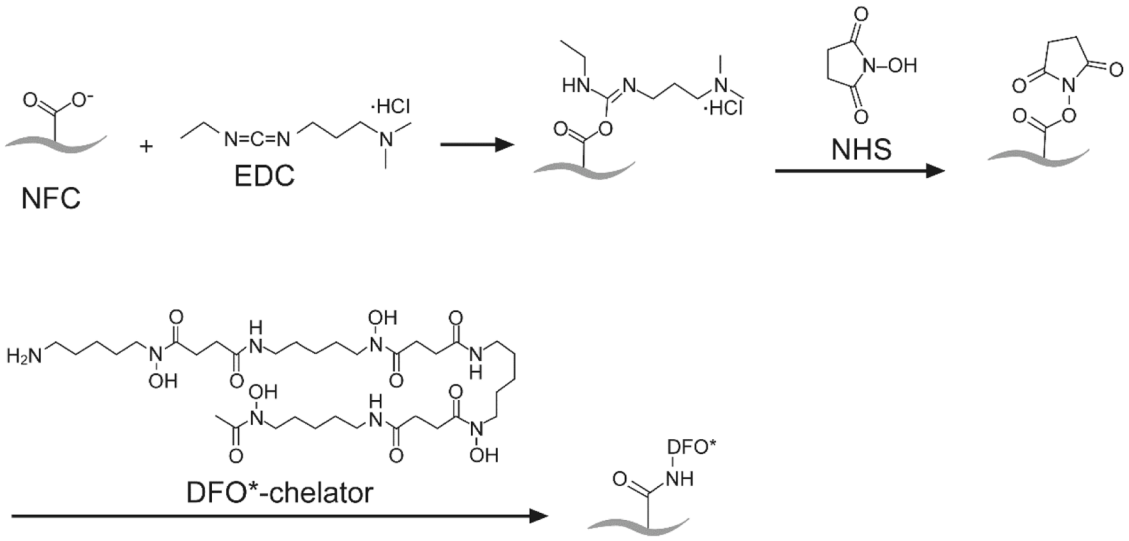

Fig. 1. Chemical scheme illustrating the conjugation of DFO* to NFC via EDC/NHS-mediated amide bond formation.

PET/CT imaging, whereas one animal was used for terminal *ex vivo* biodistribution analysis without PET/CT imaging. Animals were individually identified using ear tags, and their welfare was monitored daily throughout the study period.

2.6. In vivo PET/CT imaging

Mice were anesthetized with isoflurane (4 − 5 % for induction and 1.5 − 2 % for maintenance) (Piramal Critical Care B.V., Voorschoten, The Netherlands). In Group A, five mice (weight 19.3 ± 0.9 g, age 5.9 ± 0.0 weeks) were s.c. implanted with 3.7 ± 0.2 MBq of [^{89}Zr]Zr-DFO*-NFC (3 % w/v, 320−380 μL, pH 7 − 8) into the upper dorsal region using 25 G needles (KD Medical, Berlin, Germany). Four of the mice underwent PET/CT imaging at five different time points (Day 0, 1, 2, 7, and 14). The mice were PET imaged for 120 min on Day 0, and 40 min at other time points. In Group B, five mice (weight 19.8 ± 0.8 g, age 5.9 ± 0.0 weeks) received a s.c. implantation of 3.1 ± 0.2 MBq (220−300 μL, pH 7 − 8) of [^{89}Zr]Zr-oxalate mixed with NFC hydrogel, and four of the mice underwent PET/CT imaging at the same time points as Group A.

Imaging was performed using Molecubes PET and CT imaging systems (Molecubes NV, Gent, Belgium). High-resolution CT (50 kV, 320 μA) was performed first for attenuation correction and anatomical reference, followed by a 120-min dynamic PET acquisition on Day 0 or a 40-min static PET on all other days. CT images were reconstructed using the iterative image space reconstruction algorithm (matrix size: 200 × 200 × 200, voxel size: 0.2 × 0.2 × 0.2 mm). The PET data were reconstructed using the ordered-subsets expectation maximization algorithm with 30 iterations into 5 × 60 s and 23 × 300 s time frames (120-min dynamic) or 1 × 2400 s (40-min static) (matrix size: 192 × 192 × 384, voxel size: 0.4 × 0.4 × 0.4 mm).

The PET/CT images were analyzed using Carimas 2.10 software (Turku PET Centre, Turku, Finland, www.turkupetcentre.fi/carimas/). Regions of interest (ROIs) were defined for the implant, femur, brain, heart (including blood), kidneys, liver, lungs, muscles (bilateral forelimbs and right hindlimb), and urinary bladder content in the coronal PET/CT images, using the high-resolution CT as an anatomical reference. Transaxial and sagittal views were used to ensure correct ROI placement. Results were expressed as standardized uptake values (SUVs), in which the radioactivity concentration was normalized for the injected radioactivity dose and animal body weight, and as time-activity curves (TACs). Representative PET/CT images were extracted using Inveon Research Workplace software version 4.1 (Siemens Medical Solutions, Knoxville, TN, USA).

2.7. Ex vivo biodistribution

Ex vivo biodistribution was performed according to a previously reported protocol (Dillemuth et al., 2025). Following the final PET/CT imaging, urine samples were collected and blood samples were drawn by cardiac puncture into lithium-heparin microtubes (BD microtainer; Becton, Dickinson and Company, Franklin Lakes, NJ, USA) under deep isoflurane anesthesia. Mice were euthanized with cervical dislocation. In each group, one additional mouse was studied for *ex vivo* biodistribution without *in vivo* PET/CT imaging on the final imaging day. Immediately after the mice were euthanized, several organs were excised, weighed, and measured for total radioactivity using a Triathler 3″ gamma counter (Hidex, Turku, Finland) cross-calibrated with a VDC-405 dose calibrator (Veenstra Instruments, Joure, The Netherlands). The radioactivity of whole blood and plasma (separated by centrifugation 14,100 × *g* for 1.5 min at RT) was measured. The radioactivity concentration was decay-corrected to the time and date of injection, and the results were expressed as the percentage of injected radioactivity dose per gram of tissue (%ID/g).

2.8. Statistical analysis

The results are expressed as arithmetic means with a measure of variability (mean ± *S*.D.). Differences between groups were analyzed using the unpaired Student's *t*-test. *P* values <0.05 were considered statistically significant.

3. Results

3.1. Preparation of DFO*-NFC

On the surface of the NFC used in this study, there are carboxylic acid groups that provide an opportunity for conjugation. Generally, carboxylic acid groups are insufficiently reactive for direct conjugation. Therefore, we used a surface activation strategy by converting carboxylic acid functionality into activated esters, as previously reported (Leppiniemi et al., 2021). The activated esters subsequently reacted with the amino-functionalized DFO* chelator. The conjugation of the DFO* to NFC via EDC/NHS-mediated amide bond formation is illustrated in Fig. 1.

Since NFC cannot be readily analyzed by conventional chromatographic techniques, the progress of the conjugation reaction was monitored indirectly by HPLC analysis of DFO* consumption in the

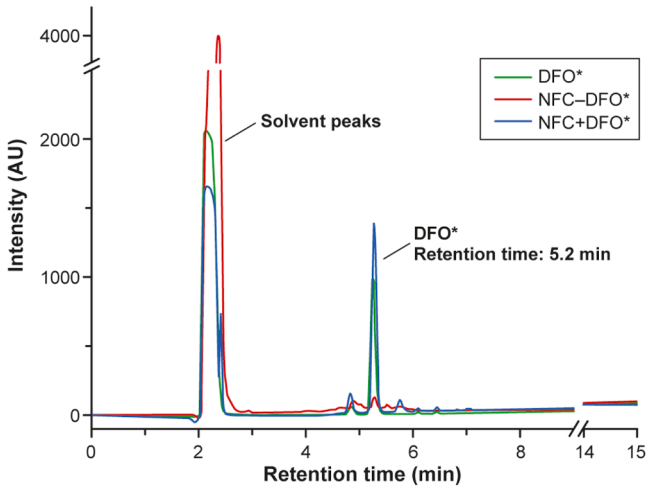

Fig. 2. HPLC analysis of NFC-DFO* conjugation. The conjugation reaction after EDC/NHS-mediated NFC activation (red trace) shows near-complete consumption of DFO*. In the control reaction without activation free DFO* (NFC + DFO*) remained at levels comparable to the reference standard (blue and green HPLC traces, respectively). HPLC conditions: Phenomenex Jupiter C18 column (5 μm, 300 Å, 150 mm × 4.6 mm); mobile phase A, H_2O with 0.1 % TFA; and mobile phase B, acetonitrile with 0.1 % TFA; gradient, 15–75 % B over 15 min; flow rate, 1 mL/min; UV detection at 220 nm.

supernatant of the reaction mixture (Fig. 2). In the reaction mixture for the preparation of NFC-DFO* using EDC/NHS activation, only trace amounts of unconjugated DFO* remained (Fig. 2, red HPLC trace) compared with the DFO* reference standard sample (Fig. 2, green HPLC trace). In contrast, when NFC and DFO* were mixed without EDC/NHS activation, the amount of unreacted DFO* was comparable to the DFO* reference standard sample (Fig. 2, blue HPLC trace). In both cases, the initial DFO* concentration was equal to that of the DFO* reference sample. These results indicate that EDC/NHS-mediated surface activation is an essential step in the conjugation of DFO* to the NFC. To purify NFC-DFO* from residual free DFO*, centrifuge-washing cycles were performed. Post-conjugation washing confirmed complete removal of unreacted DFO* after two sequential water washes, as evidenced by the absence of DFO* peaks in the wash supernatants (Fig. S1).

3.2. Preparation of [^{89}Zr]Zr-DFO*-NFC

In chelation-based radiolabeling, the labeling efficiency is often governed by the concentration of chelators (Andriana et al., 2023). In the case of NFC radiolabeling, we hypothesized that the ratio of conjugated DFO* to NFC would be a key factor influencing the labeling efficiency. To assess this, DFO* was introduced at amounts of 0.02, 0.002, 0.0002, and 0.00002 g per gram of dry NFC mass in the hydrogel. The prepared [^{89}Zr]Zr-DFO*-NFC was analyzed by TLC for chemical purity and stability. Instant TLC (iTLC) with 50 mM diethylenetriaminepentaacetic acid (DTPA) (pH 4.6) as the mobile phase clearly separated ^{89}Zr species, with [^{89}Zr]Zr-DFO*-NFC remaining at the origin (retention factor R_f = 0) and free ^{89}Zr migrating toward the solvent front (R_f = 0.8–1.0). As shown in Fig. 3, when ≤0.002 g/g dry NFC was used, free ^{89}Zr was observed within 2 h post-radiosynthesis, and increased over time. In contrast, with 0.02 g/g dry NFC, free ^{89}Zr release from the [^{89}Zr]Zr-DFO*-NFC complex was not observed for at least 24 h after radiosynthesis.

Using this optimized ratio (0.02 g DFO*/g dry NFC), [^{89}Zr]Zr-DFO*-NFC was prepared in decay-corrected radiochemical yields of 43.4 % ± 7.2 (n = 6), and with radiochemical purity of 99.3 % ± 0.2 (n = 6) as determined by TLC (Fig. 4A). [^{89}Zr]Zr-DFO*-NFC demonstrated excellent stability over 24 h: radiochemical purities were 99.33 % ± 0.15 (1 h, n = 2), 98.65 % ± 1.00 (2 h, n = 3), 99.46 % ± 0.16 (3 h, n = 2), 99.50 % ± 0.43 (12 h, n = 3), and 98.49 % ± 0.89 (24 h, n = 3). Representative TLC traces are shown in Fig. 4B Consistent stability was also observed in PBS for at least 24 h (Fig. S2).

For animal studies, 1.6 g of [^{89}Zr]Zr-DFO*-NFC (52.3 MBq, 32.7 MBq/g) was produced. As a positive control, a mixture of free [^{89}Zr]Zr-oxalate (38.2 MBq) and 1.0 g NFC hydrogel was prepared.

3.3. In vivo PET/CT imaging

The animal study design is illustrated in Fig. 5. Group A mice were s.c. implanted with [^{89}Zr]Zr-DFO*-NFC, and Group B mice were implanted with a mixture of [^{89}Zr]Zr-oxalate in NFC hydrogel. PET/CT imaging revealed distinct biodistribution patterns between the two groups.

In Group A, [^{89}Zr]Zr-DFO*-NFC hydrogel remained localized at the s.c. implant site with minimal systemic distribution (Fig. 6A). On Day 0 (within 120 min post-implantation), radioactivity was also observed in

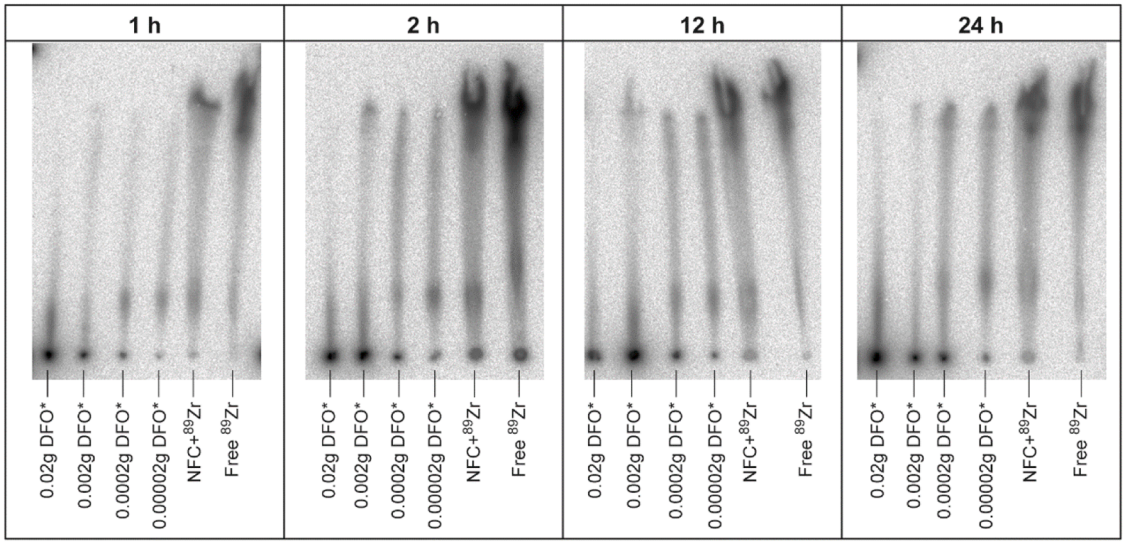

Fig. 3. TLC analysis of ^{89}Zr-labeled NFC hydrogels. Radiolabeling was assessed at 1, 2, 12, and 24 h post-labeling using NFC-DFO* prepared with varying DFO* concentrations. TLC conditions: stationary phase, silica gel iTLC strip (8 cm); mobile phase, 50 mM DTPA (pH 4.6). Retention factors: [^{89}Zr]Zr-DFO*-NFC, R_f = 0; free ^{89}Zr ([^{89}Zr]Zr-oxalate), R_f = 0.8–1.0.

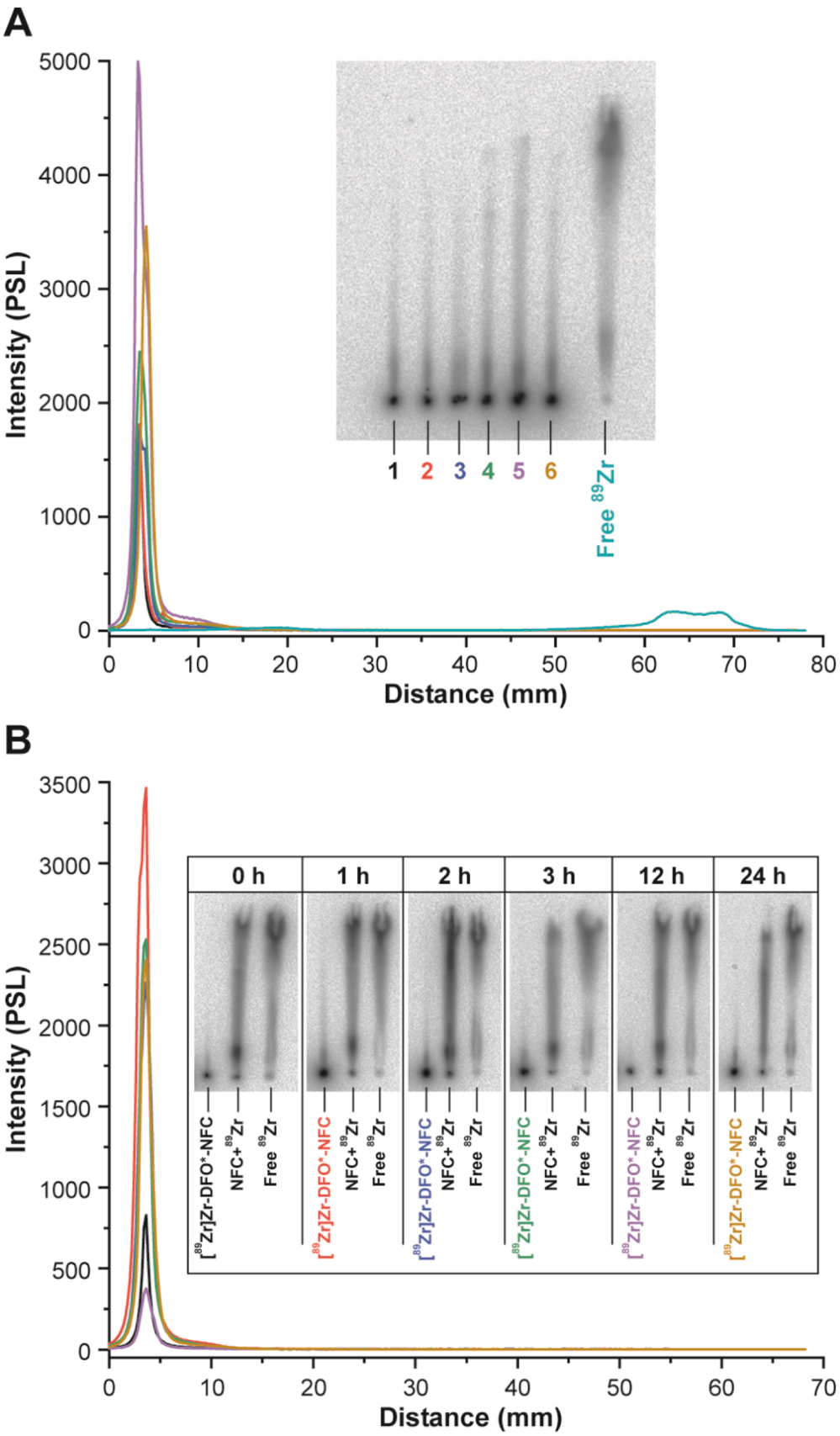

Fig. 4. TLC analysis of the radiochemical purity and stability of [^{89}Zr]Zr-DFO*-NFC. (A) Representative TLC profiles of six independent [^{89}Zr]Zr-DFO*-NFC batches (#1–6) compared with a free ^{89}Zr. (B) Stability assessment of [^{89}Zr]Zr-DFO*-NFC over 24 h post-labeling (0, 1, 2, 3, 12, and 24 h) using free ^{89}Zr and an NFC + ^{89}Zr mixture as references. TLC conditions: stationary phase, silica gel iTLC strip (8 cm); mobile phase, 50 mM DTPA (pH 4.6). Retention factors: [^{89}Zr]Zr-DFO*-NFC, R_f = 0; free ^{89}Zr ([^{89}Zr]Zr-oxalate), R_f = 0.8–1.0. PSL = photostimulated luminescence.

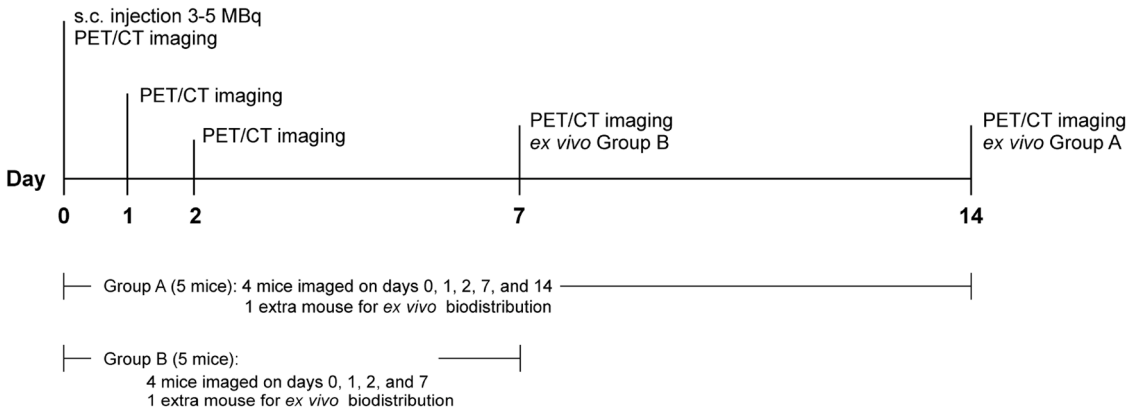

Fig. 5. Experimental design for two groups of mice: Group A, [^{89}Zr]Zr-DFO*-NFC hydrogel implants; Group B, control [^{89}Zr]Zr-oxalate + NFC hydrogel implants.

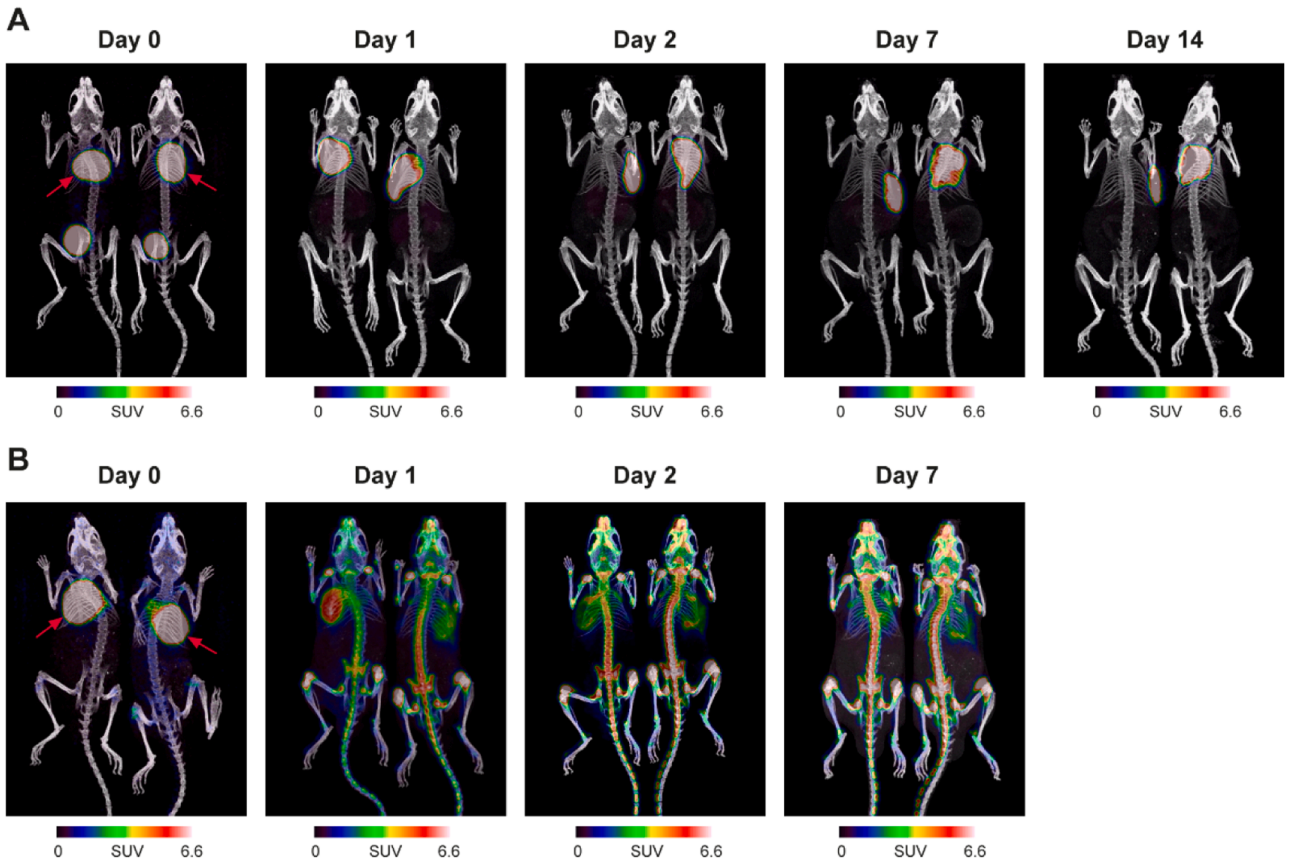

Fig. 6. Representative PET/CT images. (A) Coronal maximum intensity projection PET/CT images after s.c. implantation of [^{89}Zr]Zr-DFO*-NFC hydrogel. (B) Representative images after s.c. implantation of free ^{89}Zr ([^{89}Zr]Zr-oxalate) mixed with NFC hydrogel. Implant sites are indicated by red arrows. SUV, standardized uptake value, is defined as radioactivity concentration normalized for animal weight and injected radioactivity dose.

the urinary bladder, but this was not observed at later time points (Day 1, 2, 7, and 14), presumably due to clearance via urination. Radioactivity in the implants persisted and remained visible up to 14 days; longer monitoring was not performed.

In contrast, Group B mice implanted with a mixture of [^{89}Zr]Zr-oxalate and NFC hydrogel, showed a markedly different pattern (Fig. 6B). While radioactivity was initially confined to the implant on Day 0, subsequent PET/CT imaging revealed pronounced systemic distribution with progressive accumulation in the bones, which became increasingly intense over time.

3.4. Tissue uptake kinetics

Quantitative analysis of regional radioactivity distribution revealed markedly different kinetic profiles between Groups A and B (Fig. 7). Tissue uptake was evaluated using TACs.

In Group A, following initial washout on Day 0 (Fig. 7A), the [^{89}Zr]Zr-DFO*-NFC hydrogel maintained a stable radioactivity level at the implant site throughout the 14-day observation period, with bone uptake remaining near the background level (Fig. 7B). Minimal amounts of radioactivity were detected in the heart, liver, kidneys, and lungs, and the TACs demonstrated descending trends over time (Fig. 7C). For example, the amount of radioactivity in the liver, kidneys, and lungs

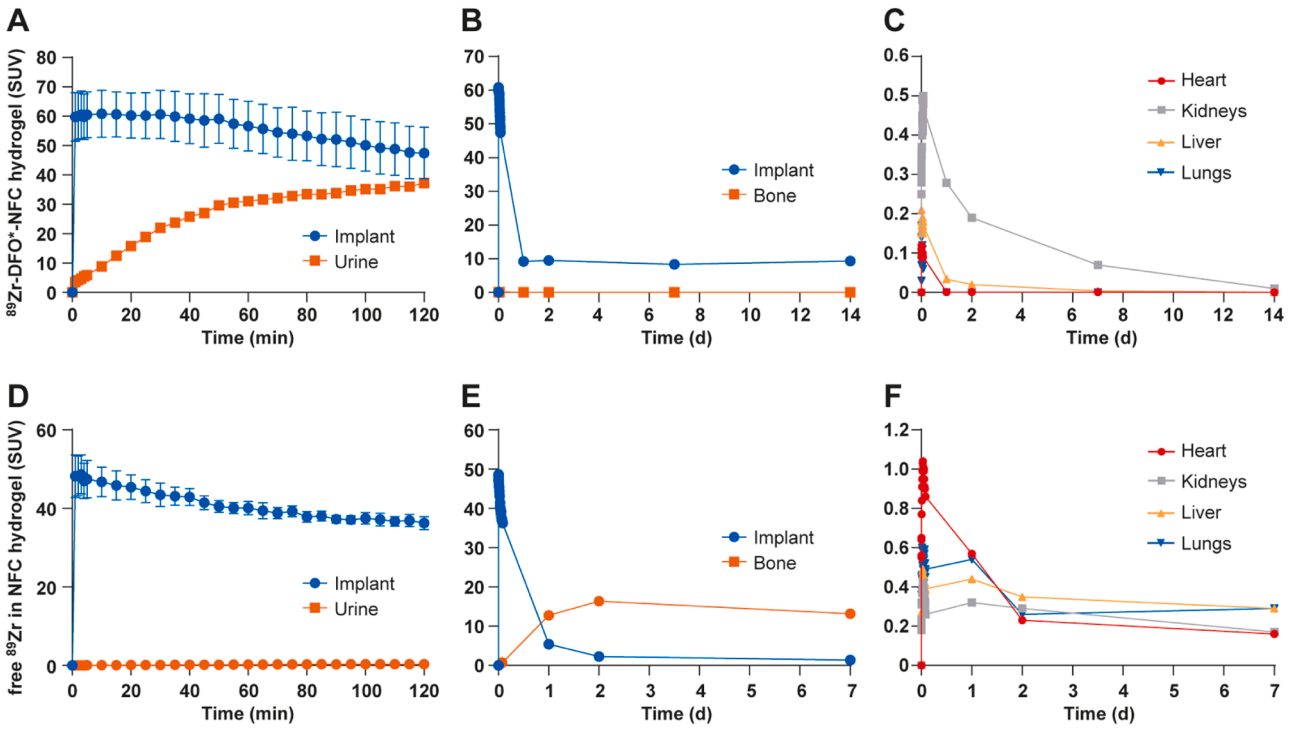

Fig. 7. Time-activity curves of regional radioactivity distribution. (A–C) s.c. implantation of [^{89}Zr]Zr-DFO*-NFC hydrogel showing sustained implant retention with minimal systemic distribution. (D–F) s.c. implantation of [^{89}Zr]Zr-oxalate in NFC hydrogel showing rapid implant clearance and progressive bone accumulation.

approached the background level by Day 2.

In Group B, by contrast, radioactivity at the implant site ([^{89}Zr]Zr-oxalate mixed with NFC hydrogel) decreased over time (Fig. 7D,E). By Day 2, radioactivity at the implantation had decreased to near the background level, while bone uptake increased significantly (Fig. 7E), which was also evident on PET/CT imaging (Fig. 6B). In the heart, liver, kidneys, and lungs, radioactivity remained at a relatively higher level from Day 2 (Fig. 7F) compared with Group A. Tables S1 and S2 provide detailed and complete time-activity data for both groups.

3.5. *Ex vivo* biodistribution

Terminal biodistribution studies were performed on Day 14 for Group A implanted with [^{89}Zr]Zr-DFO*-NFC hydrogel ($n = 5$) and on Day 7 for Group B implanted with a mixture of [^{89}Zr]Zr-oxalate and NFC hydrogel ($n = 5$) (Table 1).

In Group A, the highest radioactivity concentration was observed at the hydrogel implant site, which was ~20-fold higher than the corresponding site in Group B. Low-level radioactivity was also detected in the kidneys, skin overlying the implant, and liver, whereas most other organs were below the gamma counter's limit of detection (LoD).

In contrast, Group B ([^{89}Zr]Zr-oxalate + NFC hydrogel) showed widespread systemic distribution, with ~100-fold higher residual radioactivity in the carcass after organ removal than in Group A. The highest uptake was found in the femur (including bone marrow), skull, skin above the implant, lymph nodes, and brown adipose tissue.

For both groups, radioactivity in the adrenal glands, thymus, thyroid glands, and urine was below the LoD. In the [^{89}Zr]Zr-DFO*-NFC hydrogel group, radioactivity in nearly all other organs and tissues examined was also undetectable.

The complete organ-level data are provided in Table S3 and Table S4.

4. Discussion

One of the potential applications of NFC is its use as medical implants. Thus, evaluating the *in vivo* integrity of NFC implants is essential. This study evaluated the feasibility of ^{89}Zr-labeling of NFC hydrogel and characterize the radiolabeled s.c. implant's *in vivo* behavior. We chose the radionuclide ^{89}Zr because its relatively long physical half-life ($T_{1/2} =$ 78 h) allows longitudinal monitoring for weeks. Accordingly, we successfully prepared [^{89}Zr]Zr-DFO*-NFC hydrogel with high radiochemical purity and assessed its retention and biodistribution kinetics using quantitative radioactivity measurements following s.c. implantation in mice. A control group receiving NFC hydrogel mixed with [^{89}Zr]Zr-oxalate demonstrated the contrast between chemically conjugated and physically mixed radioactive NFC material.

The labeling protocol demonstrated that successful ^{89}Zr-conjugation requires sufficient amount of DFO* chelators conjugated on the NFC. A critical threshold of 0.02 g of DFO* per 1 g of dry NFC mass was necessary to achieve high enough labeling efficiency. This finding highlights the importance of adequate chelator concentration for efficient radiometal coordination, consistent with previous observations and radiolabeling principles (Damerow et al., 2021). The optimized formulation yielded radiochemical purity exceeding 98 % with excellent 24-h stability, suitable for preclinical imaging applications.

We showed that s.c. implantation of [^{89}Zr]Zr-DFO*-NFC using 25 G needles leveraged the semi-solid rheology of NFC hydrogel, enabling minimally invasive delivery while maintaining implant integrity. The dorsal implantation site minimized the impact on animal welfare and mobility. Throughout the 14-day observation period, all animals remained healthy with normal weight gain (~9 %), indicating excellent NFC biocompatibility and procedural tolerability. No adverse effects were observed, supporting the safety profile of NFC-based implants for biomedical applications.

PET imaging revealed distinct biodistribution phases. An initial rapid washout occurred within the first 24 h, characterized by urinary radioactivity excretion, followed by stable implant retention for the remainder of the study period. The sharp demarcation between the implant and the surrounding tissue confirmed localized material retention without significant diffusion or migration. This biphasic pattern suggests the initial elimination of small, weakly bound radioactive species, followed by stable retention of the covalently conjugated [^{89}Zr]

Table 1
Ex vivo radioactivity biodistribution (%ID/g) in male mice after s.c. implantation of [^{89}Zr]Zr-DFO*-NFC hydrogel or a mixture of [^{89}Zr]Zr-oxalate and NFC hydrogel.

	Group A (Day 14) [^{89}Zr]Zr-DFO*-NFC hydrogel (n = 5)	Group B (Day 7) [^{89}Zr]Zr-oxalate in NFC hydrogel (n = 5)	P value$^{\#}$
Implant	23.70 ± 3.41	1.21 ± 0.54	<0.0001
Adrenal glands	Below LoD	Below LoD	
Blood	Below LoD	0.03 ± 0.01	
Bone (skull)	Below LoD	9.98 ± 1.10	
Bone + marrow (femur)	Below LoD	12.85 ± 2.05	
Brain	Below LoD	0.02 ± 0.01	
Brown adipose tissue (interscapular)	Below LoD	1.03 ± 0.55	
Heart	Below LoD	0.19 ± 0.03	
Kidneys	0.23 ± 0.06	0.52 ± 0.15	0.004
Large intestine (with contents)	Below LoD	0.06 ± 0.01	
Liver	0.03 ± 0.00	0.53 ± 0.15	<0.0001
Lungs	Below LoD	0.19 ± 0.05	
Lymph node (axillary; close to implant site)	Below LoD	2.57	
Lymph node (brachial; close to implant site)	Below LoD	1.81 ± 0.20	
Lymph node (mandibular; close to implant site)	Below LoD	0.93 ± 0.09	
Muscle (right foreleg; close to implant site)	Below LoD	0.17 ± 0.09	
Muscle (left foreleg; close to implant site)	Below LoD	0.15 ± 0.04	
Muscle (right hind leg; control site)	Below LoD	0.09 ± 0.01	
Pancreas	Below LoD	0.19 ± 0.02	
Residual carcass	0.0001 ± 0.00	0.01 ± 0.00	<0.00001
Salivary glands	Below LoD	0.32 ± 0.04	
Skin (above the implant)	0.15 ± 0.02	5.60 ± 1.33	0.003
Small intestines (with contents)	Below LoD	0.05 ± 0.01	
Spleen	Below LoD	0.45 ± 0.15	
Stomach (with contents)	Below LoD	0.06 ± 0.01	
Testes	Below LoD	0.23 ± 0.08	
Thymus	Below LoD	Below LoD	
Thyroid glands	Below LoD	Below LoD	
Urine	Below LoD	ND	
White adipose tissue (gonadal)	Below LoD	0.09 ± 0.02	

Data represent terminal analysis on Day 14 for the [^{89}Zr]Zr-DFO*-NFC group and Day 7 for the [^{89}Zr]Zr-oxalate + NFC hydrogel group. The results are presented as mean ± *S*.D. LoD = limit of detection; ND = not determined; # Student's *t*-test.

Zr-DFO*-NFC matrix. Unlike water-soluble molecules, NFC forms a hydrogel in water, making it challenging to remove the weakly bound radioactive species during the purification process. The nature of the rapidly excreted radioactive species remains to be elucidated. Given that free ^{89}Zr exhibits distinct elimination kinetics (bone accumulation rather than renal excretion), the initial urinary radioactivity likely represents small molecular weight ^{89}Zr-containing species, such as incompletely conjugated DFO*-[^{89}Zr]Zr complexes or low molecular weight NFC fragments labeled with ^{89}Zr. Future studies employing HPLC-mass spectrometry analysis of urine samples could identify these species and guide the optimization of purification protocols.

The control group of mice implanted with the NFC hydrogel mixed with [^{89}Zr]Zr-oxalate demonstrated fundamentally different pharmacokinetics, with a slower initial clearance from the implant site but extensive systemic redistribution. The predominant bone accumulation pattern is characteristic of free ^{89}Zr, which exhibits a high affinity for calcium phosphate minerals in skeletal tissue (Abou et al., 2011). This control group effectively validated our experimental approach by confirming that the stable implant retention observed with [^{89}Zr]Zr-DFO*-NFC resulted from chemical conjugation rather than simple physical entrapment. *Ex vivo* tissue analysis corroborated the imaging findings. Radioactivity at the [^{89}Zr]Zr-DFO*-NFC implant site was ~20-fold higher compared with the control group (23.70 *vs.* 1.21 %ID/g). The minimal off-target distribution was detected in kidneys (0.23 %ID/g) and overlying skin (0.15 %ID/g), confirming the localized nature of this biomaterial platform. Conversely, the control group exhibited widespread tissue distribution, particularly in bone (femur: 12.85 %ID/g; skull: 9.98 %ID/g), reflecting the systemic bioavailability of free ^{89}Zr, and validated our conjugation strategy.

Our results align with those of a previous study by Laurén et al. (2014), and their results demonstrated the stable retention of ^{99m}Tc-labeled NFC hydrogel for 5 h using SPECT imaging. Our study extends these findings by providing longer observation periods (14 days *vs.* 5 h), higher sensitivity imaging (PET *vs.* SPECT), and comprehensive biodistribution analysis. The consistency between studies using different radiotracers and imaging modalities strengthens confidence in the general stability and biocompatibility of radiolabeled NFC hydrogels.

These findings have important implications for clinical development. The demonstrated biocompatibility, localized retention, and minimal systemic exposure show favorable characteristics for various therapeutic applications. Noninvasive PET tracking enables the monitoring of implant fate and treatment protocol optimization. Future investigations should include larger, sex-inclusive cohorts and disease-relevant models to enable mechanistic studies on implant stability and biocompatibility. Applying this radiolabeling approach to disease models, such as wound healing or oncology settings, will help determine whether pathological conditions accelerate degradation, alter clearance, or shift biodistribution. Such studies will provide important insights into the versatility of NFC hydrogel for targeted clinical applications. The integration of complementary imaging modalities and advanced analytical techniques could provide deeper insights into material-tissue interactions and guide further optimization of NFC hydrogel preparation.

5. Conclusion

This study demonstrates the feasibility of preparing a stable ^{89}Zr-labeled NFC hydrogel that exhibits excellent localized *in vivo* retention with minimal systemic distribution. The validated radiolabeling approach enhances the safety profiling and traceability of NFC hydrogel, supporting its potential use as a biocompatible medical device for subcutaneous applications such as drug delivery and tissue engineering. Future work should focus on evaluating its performance in disease models to facilitate clinical translation.

Funding

This work was supported by research funding from UPM Biomedicals, Helsinki, Finland.

CRediT authorship contribution statement

Xiaoqing Zhuang: Writing – review & editing, Writing – original draft, Visualization, Validation, Methodology, Investigation, Formal analysis, Data curation. **Jenni Virta:** Writing – review & editing, Writing – original draft, Methodology, Investigation, Formal analysis, Data curation. **Heidi Liljenbäck:** Writing – review & editing, Methodology, Data curation. **Lauri Paasonen:** Writing – review & editing, Visualization, Supervision, Resources, Funding acquisition, Conceptualization. **Anu J. Airaksinen:** Writing – review & editing, Supervision, Investigation, Conceptualization. **Anne Roivainen:** Writing – review & editing, Writing – original draft, Visualization, Supervision, Formal analysis, Conceptualization. **Xiang-Guo Li:** Writing – review & editing, Writing – original draft, Visualization, Validation, Supervision, Resources, Project administration, Methodology, Investigation, Funding acquisition, Formal analysis, Data curation, Conceptualization.

Declaration of competing interest

The authors declare no competing interests.

Acknowledgements

The authors thank Aake Honkaniemi for technical support, and Timo Kattelus for finalizing figures.

Supplementary materials

Supplementary material associated with this article can be found, in the online version, at doi:10.1016/j.ejps.2025.107402.

Data availability

Data are available upon reasonable request.

References

Abou, D.S., Ku, T., Smith-Jones, P.M., 2011. *In vivo* biodistribution and accumulation of ^{89}Zr in mice. Nucl. Med. Biol. 38, 675–681. https://doi.org/10.1016/j.nucmedbio.2010.12.011.

Andriana, P., Makrypidi, K., Liljenbäck, H., Rajander, J., Saraste, A., Pirmettis, I., Roivainen, A., Li, X.-G., 2023. Aluminum fluoride-18 labeled mannosylated dextran: radiosynthesis and initial preclinical positron emission tomography studies. Mol. Imaging Biol. 25, 1094–1103. https://doi.org/10.1007/s11307-023-01816-7.

Chomet, M., Schreurs, M., Bolijn, M.J., Verlaan, M., Beaino, W., Brown, K., Poot, A.J., Windhorst, A.D., Gill, H., Marik, J., Williams, S., Cowell, J., Gasser, G., Mindt, T.L., van Dongen, G.A.M.S., Vugts, D.J., 2021. Head-to-head comparison of DFO* and DFO chelators: selection of the best candidate for clinical ^{89}Zr-immuno-PET. Eur. J. Nucl. Med. Mol. Imaging 48, 694–707. https://doi.org/10.1007/s00259-020-05002-7.

Damerow, H., Hübner, R., Judmann, B., Schirrmacher, R., Wängler, B., Fricker, G., Wängler, C., 2021. Side-by-side comparison of five chelators for ^{89}Zr-labeling of biomolecules: investigation of chemical/radiochemical properties and complex stability. Cancers (Basel) 13, 6349. https://doi.org/10.3390/cancers13246349.

Dillemuth, P., Ayo, A., Airenne, T.T., Lövdahl, P., Bakay, E., Zhuang, X., Liljenbäck, H., Paunonen, S.T., Kunnas, J., Filppu, P., Rajander, J., Johnson, M.S., Roivainen, A., Salminen, T.A., Rosenholm, J.M., Laakkonen, P., Li, X.-G., 2025. Utilizing monocarboxylate transporter 1-mediated blood–brain barrier penetration for glioblastoma positron emission tomography imaging with 6-[^{18}F]fluoronicotinic acid. Mol. Pharm. 22, 4819–4830. https://doi.org/10.1021/acs.molpharmaceut.5c00457.

Feiner, I.V.J., Brandt, M., Cowell, J., Demuth, T., Vugts, D., Gasser, G., Mindt, T.L., 2021. The race for hydroxamate-based zirconium-89 chelators. Cancers (Basel) 13, 4466. https://doi.org/10.3390/cancers13174466.

Gil, C.J., Tomov, M.L., Theus, A.S., Cetnar, A., Mahmoudi, M., Serpooshan, V., 2019. *In Vivo* tracking of tissue engineered constructs. Micromachines (Basel) 10, 474. https://doi.org/10.3390/mi10070474.

Koivuniemi, R., Hakkarainen, T., Kiiskinen, J., Kosonen, M., Vuola, J., Valtonen, J., Luukko, K., Kavola, H., Yliperttula, M., 2020. Clinical study of nanofibrillar cellulose hydrogel dressing for skin graft donor site treatment. Adv. Wound Care (New Rochelle) 9, 199–210. https://doi.org/10.1089/wound.2019.0982.

Laurén, P., Lou, Y.-R., Raki, M., Urtti, A., Bergström, K., Yliperttula, M., 2014. Technetium-99m-labeled nanofibrillar cellulose hydrogel for *in vivo* drug release. Eur. J. Pharm. Sci. 65, 79–88. https://doi.org/10.1016/j.ejps.2014.09.013.

Leppiniemi, J., Mutahir, Z., Dulebo, A., Mikkonen, P., Nuopponen, M., Turkki, P., Hytönen, V.P., 2021. Avidin-conjugated nanofibrillar cellulose hydrogel functionalized with biotinylated fibronectin and vitronectin promotes 3D culture of fibroblasts. Biomacromol 22, 4132–4137. https://doi.org/10.1021/acs.biomac.1c00579.

Malekpour, K., Hazrati, A., Khosrojerdi, A., Roshangar, L., Ahmadi, M., 2023. An overview to nanocellulose clinical application: biocompatibility and opportunities in disease treatment. Regen. Ther. 24, 630–641. https://doi.org/10.1016/j.reth.2023.10.006.

Mishra, P.K., Pavelek, O., Rasticova, M., Mishra, H., Ekielski, A., 2022. Nanocellulose-based biomedical scaffolds in future bioeconomy: a techno-legal assessment of the State-of-the-art. Front. Bioeng. Biotechnol. 9, 789603. https://doi.org/10.3389/fbioe.2021.789603.

Pawelec, K.M., Hix, J.M.L., Troia, A., Kiupel, M., Shapiro, E.M., 2024. Material composition and implantation site affect *in vivo* device degradation rate. bioRxiv [Preprint] 2024.09.09.612079. https://doi.org/10.1101/2024.09.09.612079.

Sultan, S., Siqueira, G., Zimmermann, T., Mathew, A.P., 2017. 3D printing of nano-cellulosic biomaterials for medical applications. Curr. Opin. Biomed. Eng. 2, 29–34. https://doi.org/10.1016/j.cobme.2017.06.002.

Wang, L., Li, K., Copenhaver, K., Mackay, S., Lamm, M.E., Zhao, X., Dixon, B., Wang, J., Han, Y., Neivandt, D., Johnson, D.A., Walker, C.C., Ozcan, S., Gardner, D.J., 2021. Review on nonconventional fibrillation methods of producing cellulose nanofibrils and their applications. Biomacromolecules 22, 4037–4059. https://doi.org/10.1021/acs.biomac.1c00640.